Supporting Information

Harnessing Thermoelectric Puddles *via* the Stacking Order and Electronic Screening in Graphene

Mali Zhao[†], Dohyun Kim[†], Yongjoon Lee[†], Ning Ling[†], Shoujun Zheng[†], Young Hee Lee[†,‡], and Heejun Yang[ƨ]*

[†]Department of Energy Science, Sungkyunkwan University, Suwon 16419, Korea

[‡]Center for Integrated Nanostructure Physics (CINAP), Institute for Basic Science, Suwon 16419, Korea

[ƨ]Department of Physics, Korea Advanced Institute of Science and Technology, Daejeon 34141, Korea

*Correspondence: h.yang@kaist.ac.kr

1. Sample preparation and characterization before and after the SThEM measurement

The single-layer graphene device was fabricated by typical nanodevice fabrication procedure, and an OM image of the nanodevice with two Cr/Au electrical contacts is shown in **Figure S1**a. After fabrication of the graphene device, a part of the PMMA residual is left on the graphene surface, which dramatically degrades the device performance and hinders the thermoelectric mapping of the pristine clean graphene surface, see **Figure S1**b. To remove the PMMA, an AFM cantilever in contact mode with a strong force of 36 nN was used. After the cantilever cleaning step, most of the PMMA was successfully removed and the graphene topography becomes clean enough for STM and thermopower mapping, see **Figure S1**c. We note that a local strip-like feature marked in the dashed square, which corresponds to the boundary in **Figure 1**b, is observed. The line profile shows a height variation of 7.96 Å between the strip-like feature and the surrounding single layer graphene (SLG) area, which is similar to the double graphene interlayer distance (6.70 Å). The entire AFM image supports our claim that the strip-like feature is a trilayer graphene (TLG) region. The transport measurement for the sample after cantilever cleaning was conducted using a probe station under a high vacuum (10^{-6} torr). The minimum conductance as a function of the back-gate voltage shows that the average charge neutrality point (CNP) is at -0.62 V, indicating a relative neutral doping level. The residual charge carrier density $n_0 = \alpha V_0$ is estimated to be 4.68×10^{10} cm^{-2}, where, $\alpha = 7.563\times10^{10}\,cm^{-1}V^{-1}$. Based on the Drude model, $\sigma = en\mu$, (where, n is the sheet carrier density, and σ is the sample conductivity), we fitted the two-terminal conductance as a function of the back-gate voltage, yielding graphene sheet mobility μ of 3000-4000 $cm^2V^{-1}s^{-1}$. Hysteresis is observed in the transfer curve due to the trapped charges in graphene when conducting gate sweeping.[1] After annealing the sample in a UHV chamber at 150 °C for three hours to remove any possible adsorbed water and other molecules, the *in-situ* multi-terminal electrical transport measurement was taken by connecting Cr/Au electrodes and the exposed Si layer to the electrical terminals on the sample stage *via* wire bonds. The conductance minimum is shifted to -58.8 V, indicating high *n*-type doping of the graphene sheet; the residual charge carrier density is increased to 4.17×10^{12} cm^{-2}.

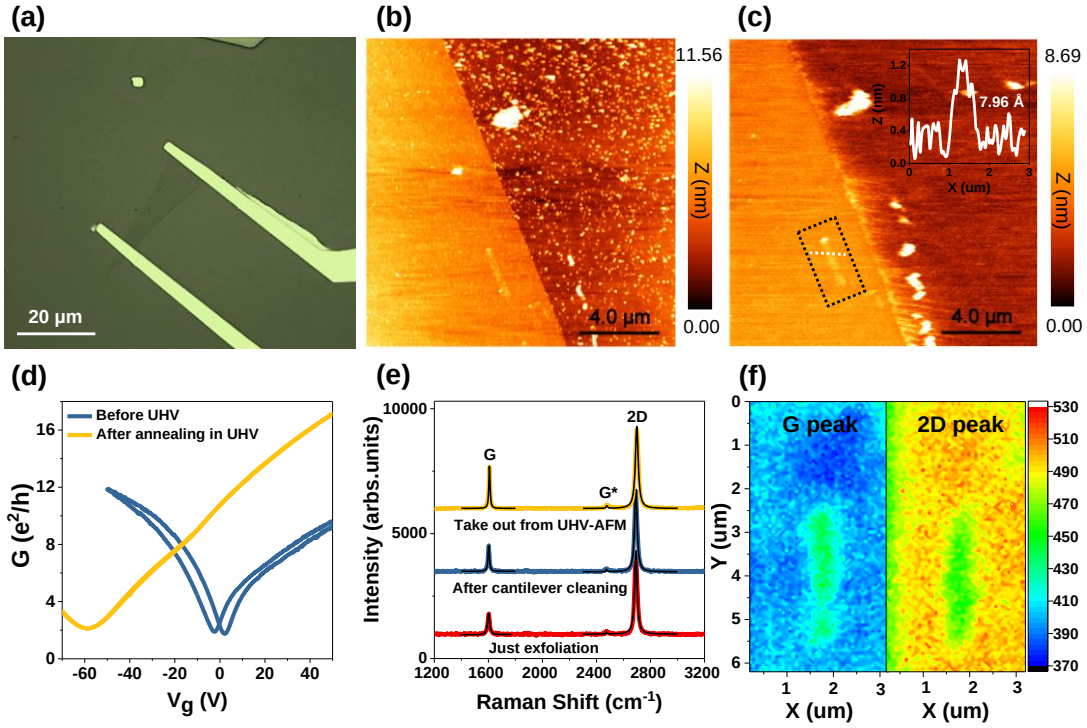

Figure S1. Sample characterization before and after the SThEM measurement. (a) OM image of the mechanical exfoliated SLG/SiO_2 device. **(b)** Topography image of the exfoliated graphene obtained by ambient dynamic force microscopy (DFM). **(c)** Topography image of a graphene sheet after AFM cantilever cleaning (15.4 μm×15.4μm). The PMMA residual on the sample surface is successfully removed. The inset line profile indicates the height difference between strip-like feature and the surrounding SLG sheet is 7.96 Å. **(d)** Source-drain current as a function of the back-gate voltage for the graphene device. The blue line is the transfer curve for the graphene device after cantilever cleaning, as obtained under a high vacuum (10^{-6} torr). The yellow curve is the *in-situ* electrical transport measurement in the UHV. **(e)** Single-point Raman spectroscopy on graphene. **(f)** 6.2 um × 3.2 um Raman mapping of the G peak and 2D peak intensity in the rectangular dashed region in panel **(c)**.

Raman spectroscopy was conducted to characterize the mechanically exfoliated graphene on SiO_2 before and after transferring the sample to the UHV chamber (see **Figure S1**e). For pristine graphene, a D peak is not observed. G and 2D (second-order Raman scattering in graphene) peaks are found at 1602.52 cm^{-1} and 2690.83 cm^{-1}, respectively. The intensity ratio between the 2D peak and the G peak (I_{2D}/I_G) is 3.94, indicating high-quality crystallinity of the graphene. After AFM cantilever cleaning,

the G peak and 2D peak mostly do not change (1602.68 and 2691.30 cm^{-1}, respectively); the intensity ratio of (I_{2D}/I_G) is decreased slightly to 2.91 but is still higher than 2, indicating that the AFM cantilever does not destroy the crystallinity of graphene. After the SThEM measurement in the UHV, Raman spectroscopy was immediately conducted after taking the sample out of the UHV-chamber. The I_{2D}/I_G ratio was found to have decreased to 1.94. The G peak and 2D peak are blue-shifted to 1607.59 ($\omega\Delta_G$=5.23) and 2698.52 cm^{-1} ($\omega\Delta_{2D}$=6.16), respectively, which gives a position shift ratio $\omega\Delta_{2D}/\omega\Delta_G$ of 1.18, less than 2.21, illustrating that both the compressive strain and charge doping levels are increased after annealing.[2-5] In the Raman mapping shown in **Figure S1**f, the intensity ratio of I_{2D}/I_G near the thicker layer is slightly less than one, suggesting that the local thick area is trilayer graphene. The stacking order in TLG cannot easily be determined in the Raman mapping, due to the small TLG domain size and the limited laser resolution (~200 nm).

2. STM and STS measurement on graphene with different layers and stacking orders

Due to the charge fluctuation in the exfoliated graphene sheet on SiO_2, the local Dirac point is energetically shifted with respect to the global charge neutrality point (CNP). To determine the intrinsic electronic band structure in the studied area precisely, the dI/dV spectra were taken over an area of 100 nm ×100 nm of the SLG and ABA- and ABC-stacked TLGs, respectively, as indicated by the red, blue, and yellow dashed frames in **Figure S2**a. The average 1600 spectra curves on each region are shown in **Figure S2**b. For the SLG, the spectra show a local minimum at -0.415 eV, caused by the alignment of the tip Fermi level and the local Dirac point of graphene, consistent with the nature of highly *n*-type doping in transport measurements in a UHV. Compared to the overall CNP at -58.8 V in the transport measurement, the tip effect in STS must be considered. In principle, the differential tunneling conductance on graphene at T=0 K is proportional to the DOS. Due to the linear dispersion in the SLG near the Dirac point, the DOS could be expressed by the equation $N_{E=eV_b} = \frac{2|eV_b - E_D|}{\pi\hbar^2 v_F^2}$, where $\hbar$ is the reduced Planck constant and υ_F is the Fermi velocity of graphene[6], which is about 1.1 $\times 10^{-6}$ ms^{-1}. Due to the work function mismatch between the tip and the sample, the potential difference would be the corresponding contact potential difference V_{CPD}, instead of zero. Therefore, the effective potential difference between the two is V_b-V_{CPD}, when a bias voltage V_b is applied. When a back gate is applied on Si, the total carrier density induced in graphene due to the metallic tip and back gate can be written as: $n = \frac{k\varepsilon_0}{etz_{ts}}(V_g - \beta(V_b - V_{CPD}))$, where, $k = 3.9$ is the dielectric constant of the SiO_2, t=300 nm, is the gate oxide thickness, ε_0 is the vacuum permittivity, z_{ts} is the tip-sample distance (0.5~1.0 nm), $\beta = t/kz_{ts}$, $V_{CPD} = \frac{\Delta + E_D}{e}$, and Δ is the work function difference between the charge neutrality graphene and the tip. As a result, the local Dirac point shift induced by the metal tip and back-gate can be estimated by the equation:[7, 8]

$E_D = -\frac{\gamma e}{2} sign(v)(-\beta\gamma + \sqrt{4|v| + \beta^2\gamma^2})$, where, $\gamma = \hbar v_F \sqrt{\frac{\pi k\varepsilon_0}{e^3 t}} = 0.031$, $v = V_g - \beta(V_b - \Delta)$. In the STS shown in **Figure S2**b, a Pt/Ir (10%) tip with a diameter of 0.25 mm and work function of -5.1 eV

was used, and the set-point sample bias V_b was -0.5 V. Therefore when the gate voltage is zero, the calculated Dirac point energy ranges from -0.11 eV to -0.09 eV in the tunneling range. In other words, the tip-sample work function mismatch causes the detected Dirac point to shift to approximately 0.1 eV lower than the Fermi level. For the TLG, a typical V-shaped spectrum is evident in the upper region (blue curve), and no bandgap or Dirac point shift is detected. In contrast, the STS curve on the lower region shows a weak peak at +0.18 eV. The difference between the two spectra demonstrate that the TLG is heterogeneous in electronic structures. The band structure of the TLG can be understood as a combination of Bernal stacked bilayer graphene with parabolic bands and single-layer graphene with a linear dispersion. Owing to different stacking orders, the band structure in the TLG could be distinct. The spectrum in the upper region is consistent with the metallic feature of the TLG with ABA (Bernal) stacking. The spectrum in the lower region is a typical feature in a TLG with ABC (rhombohedral) stacking, where the peak at +0.18 eV is the flat band-induced DOS peak,[9-11] indicating slight *p*-type doping. Due to thermal smearing near room temperature, the flat band induced DOS peak is weaker than that measured at a low temperature.

After the thermoelectric measurement, the STS spectrum was obtained on the zoomed 140 nm × 140 nm area near the wrinkle (see the black square frame in **Figure S2**a and the topography image in **Figure S2**c). The dI/dV mapping shown in **Figure S2**d exhibits a sharp DOS variation at the starting line of the upper wrinkle in the topography, where the upper TLG with ABA-stacking shows a higher DOS than the lower area with ABC-stacking at a sample bias of -0.2 V. The spectroscopy across the line profile in **Figure S2**d demonstrates the sharp ABA to ABC-stacking order transition (see **Figure S2**e).

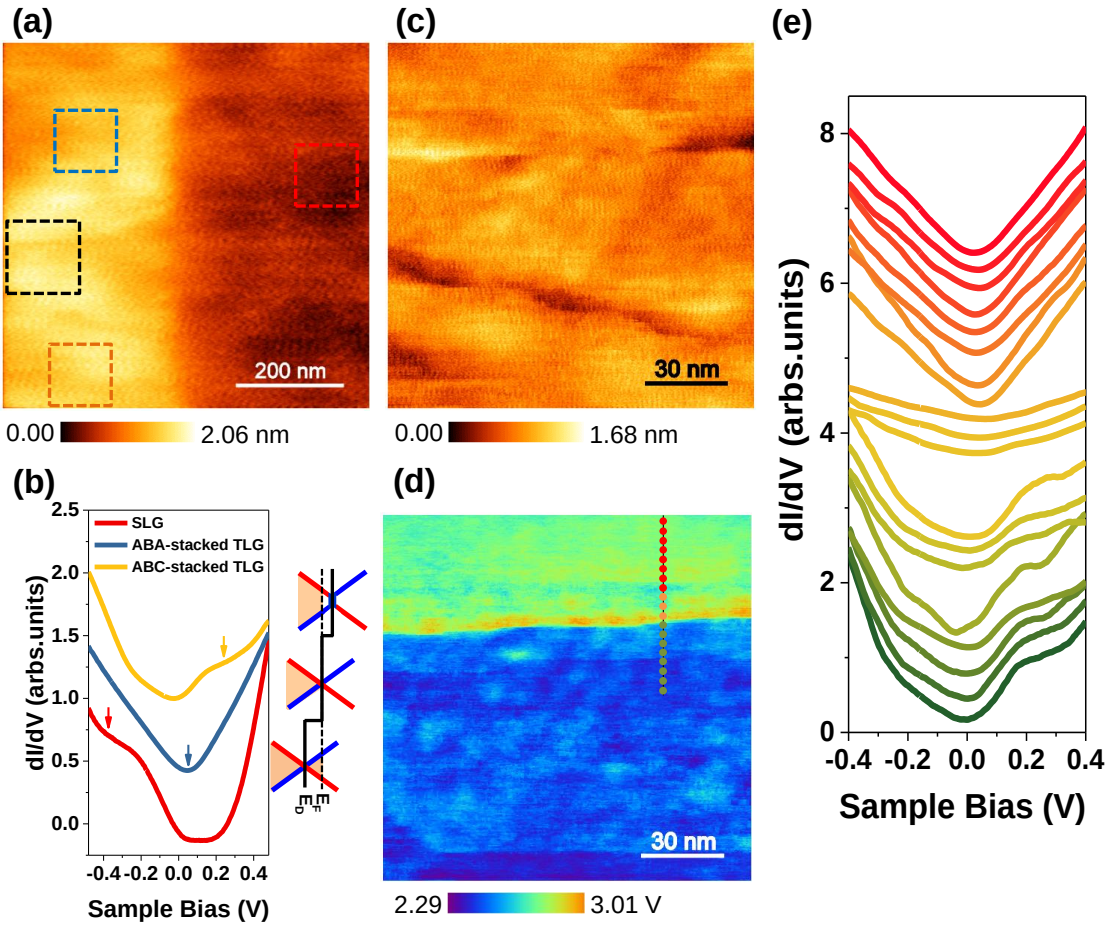

Figure S2. STM and STS measurement on graphene with different stacking orders. (a) Topography image of the SLG and TLG with dimensions of 700 nm×700 nm. **(b)** The STS on graphene shows that the conductance minima in the SLG, the ABA-stacked TLG, and the ABC-stacked TLG are close to -0.415 eV, 0.04 eV, and +0.24 eV, respectively, with respect to the Fermi level. The spectra curves are vertically shifted for better clarify. **(c)** Zoomed topography image of the TLG with the ABA and ABC domain wall transition region in panel (a) (140 nm×140 nm). **(d)** Simultaneously obtained dI/dV mapping outcomes in the TLG with the ABA-ABC domain wall transition region. The upper TLG (ABA-stacking) exhibits a higher DOS than that in the lower TLG (ABC-stacking). Scanning condition: V_s=-0.2 V, raster time=12 ms. **(e)** A series of dI/dV spectra curves along the line profile in panel **(d)**.

3. Topography, thermopower and dI/dV mapping comparison in SThEM and STM.

To better clarify the correlation between topography and thermopower fluctuation, the topography in STM and SThEM as well as the dI/dV and thermpower mappings are compared. **Figure 3**a shows the AFM topography (100 nm×100 nm) image of SLG/SiO_2. The RMS roughness is 181.7 pm and the maximum height is 1.68 nm. The STM topography image of SLG/SiO_2 with the same size (100 nm× 100 nm) at the similar location (**Figure S3**c) displays both the RMS roughness (171.7 pm) and the maximum height (1.30 nm) are slightly smaller than that obtained by AFM. In addition, the topography spatial distribution in AFM and STM are distinctly different. In contrast, thermopower (**Figure S3**b) and dI/dV mappings (**Figure S3**d) exhibit the similar contour, demonstrating the same origin of the contrast in thermopower mapping ($S \propto (\ln DOS)'$) and dI/dV mapping ($\propto DOS$), that is the DOS variation in the proximity of the Fermi level.

The topography difference are caused by the different working principle of AFM and STM. In STM imaging with constant current feedback loop, the corrugation of the surface could be expressed by $\Delta z(r) = -\frac{\Delta I(r)}{dI_0(z)/dz}$, where, $I_0(z)$ is the set-point tunneling current, $\Delta I(r)$ is a small variable current at a local site. According to the Tersoff-Hamann model, tunneling current is equal to $I \propto \int_0^{eV} \rho_s(E_F + \varepsilon, r) d\varepsilon$, where, ρ_s is the DOS of the sample. Therefore, the constant current topography image is affected by both the topography height and the sample DOS over an energy range of [E_F, E_F+eV].

In contrast, the topography is imaged in AFM with constant force feedback loop. The contrast of the surface is $\Delta z(r) = -\frac{\Delta F(r)}{dF_0(z)/dz}$, where, $F_0(z)$ is the set-point force between tip and sample, $\Delta F(r)$ is a small variable force at a local site. The van der Waals interaction energy between a tip and a sample surface is $U = -\frac{HR_c}{6z(r)}$, where, $H \equiv \pi^2 C \rho_1 \rho_2$ is the Hamaker constant, C is the force constant, ρ_1 and ρ_2 are the density of atoms of the tip and sample, respectively. R_c is the radius of the tip apex, *z(r)*

is the distance from the tip apex to the sample surface. Therefore, the constant force topography image only reflects the variation of the tip-sample distance, in other words, the surface height corrugation.

The cross-correlation coefficient (NCC) between STM topography and dI/dV mapping (0.65) as well as AFM topography and thermopower mapping (0.38) also confirms the STM topography has strong correlation with DOS variation. To study the origin of the local thermopower fluctuation (from topography corrugation or charged states), it is of significance to obtain the pure topography height variation by AFM, instead of STM.

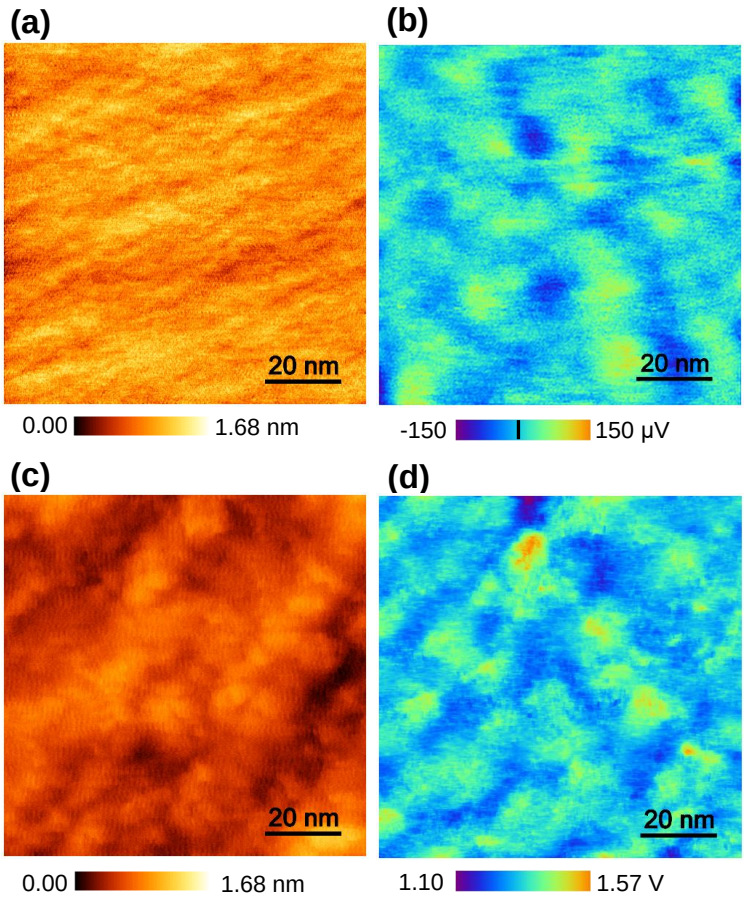

Figure S3. Topography, thermopower and dI/dV mappings by SThEM and STM. (a) AFM topography (100 nm × 100 nm) image of SLG/SiO_2. F=0.0005 nN. **(b)** Simultaneously obtained thermopower mapping (V_g=0 V, ΔT=60 K). **(c)** STM topography (100 nm × 100 nm) image of SLG/SiO_2. V_s=-0.4 V, I=0.3 nA. **(d)** Simultaneously obtained dI/dV mapping by lock-in amplifier (658.7 Hz with a modulation voltage of 20 mV). The scale bar is an arbitrary unit.

4. Charge-impurity-induced thermoelectric puddles in the SLG at different back-gate voltages

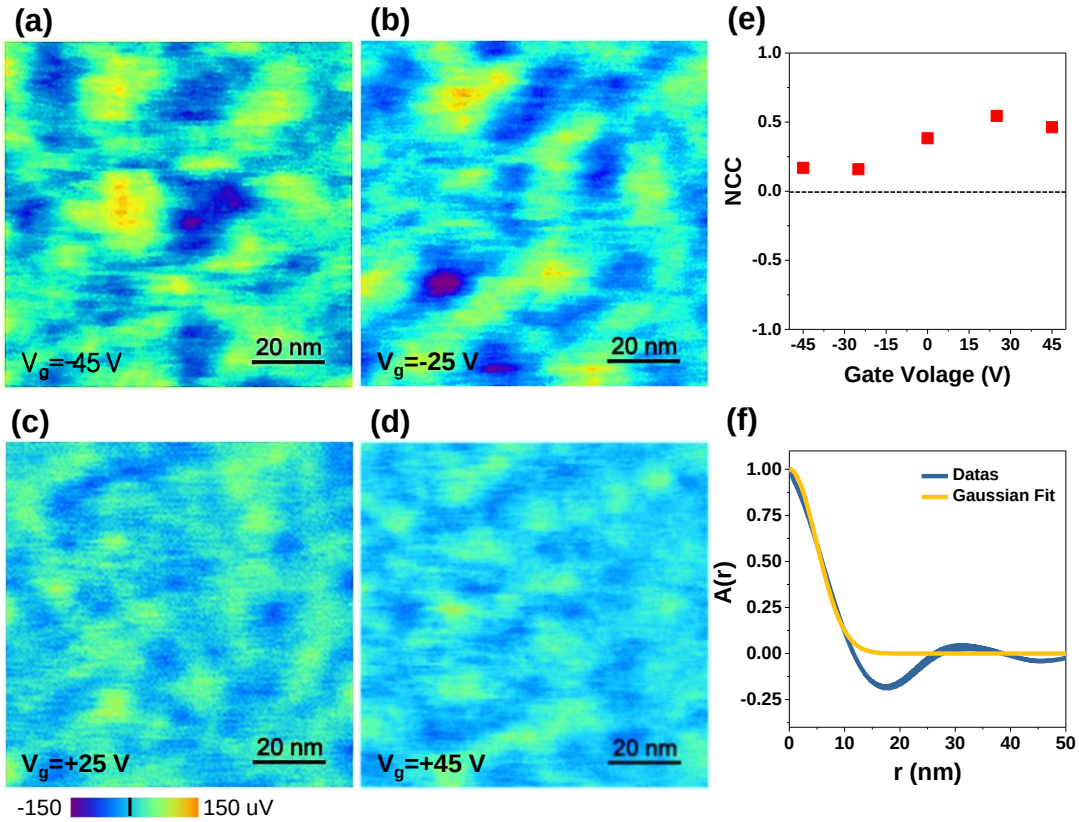

Figure S4. Thermoelectric puddles of SLG (100 nm×100 nm) at different back-gate voltages. From panel **(a)** to **(d)**, the back-gate voltage is -45 V, -25 V, +25 V, and +45 V, respectively (ΔT=60 K). The scale bar is not the actual thermoelectric voltage, instead, it represents the thermoelectric voltage deviation from the mean value in the scanned region. The corresponding topography image is Figure 2a in the main text. **(e)** The normalized cross-correlation coefficient (NCC) between topography and thermoelectric puddles with respect to the gate voltage. The NCC ranges from 0.16 to 0.54 with the charge carrier concentration, suggesting the thermoelectric puddles are partially correlated with the topography. **(f)** The angular averaged normalized auto-correlation A(r) of the thermoelectric puddles in panel **(b)**. The yellow line is the Gaussian fit of the experimental data.

Extraction of the thermoelectric puddle correlation length

The thermoelectric puddle dimension is defined as the auto-correlation length, which could be obtained from the normalized auto-correlation of each thermopower image. Specifically, the auto-correlation matrix of the thermoelectric voltage mapping can be expressed as follows:

$$C(i,j)=\frac{\sum_{m=1}^{M}\sum_{n=1}^{N}[\Delta V(m,n)-<\Delta V>][\Delta V(m+i,n+j)-<\Delta V>]}{M\times N},$$

Dividing C(i,j) by the central element, C(0,0), we can obtain the normalized auto-correlation matrix A(r,φ). After drawing a line cut in the auto-correlation matrix along a fixed direction φ, we can obtain the angular average line cut of A(r) (see the blue line in **Figure S3**f). Fitting this curve with a Gaussian function $A(r)=e^{-r^2/2\xi^2}$ (indicated in the yellow line in **Figure S3**f) gives the average decay length ξ of the correlation curve, which could characterize the lateral dimension of the thermoelectric puddles.

Normalized cross-correlation (NCC) calculation

To explore the origin of the thermoelectric puddles, the normalized cross-correlation (NCC) between the topography ($f(\vec{r})$) and the thermopower mapping ($g(\vec{r})$) was analyzed[12] using the equation below:

$$C_{f,g}(\vec{R}=0)=\frac{\int[f(\vec{r})-\langle f\rangle]\times[g(\vec{r}+\vec{R})-\langle g\rangle]d^2r}{\sqrt{A_{f,f}(0)A_{g,g}(0)}}$$

Here, $A_{f,f}(\vec{R})=\int[f(\vec{r})-\langle f\rangle]\times[f(\vec{r}+\vec{R})-\langle f\rangle]d^2r$. The identical images yield $C_{f,g}(0)=1$; an image with its reverse gives $C_{f,g}(0)=-1$. If $C_{f,g}(0)=0$, and the images do not correlate at all. Compared to the topography in the STM, which contains certain DOS information due to the constant current feedback-loop during scanning, the topography in the conductive AFM reflects the actual surface corrugation.

5. Strain-induced thermoelectric puddles in the SLG at different back-gate voltages

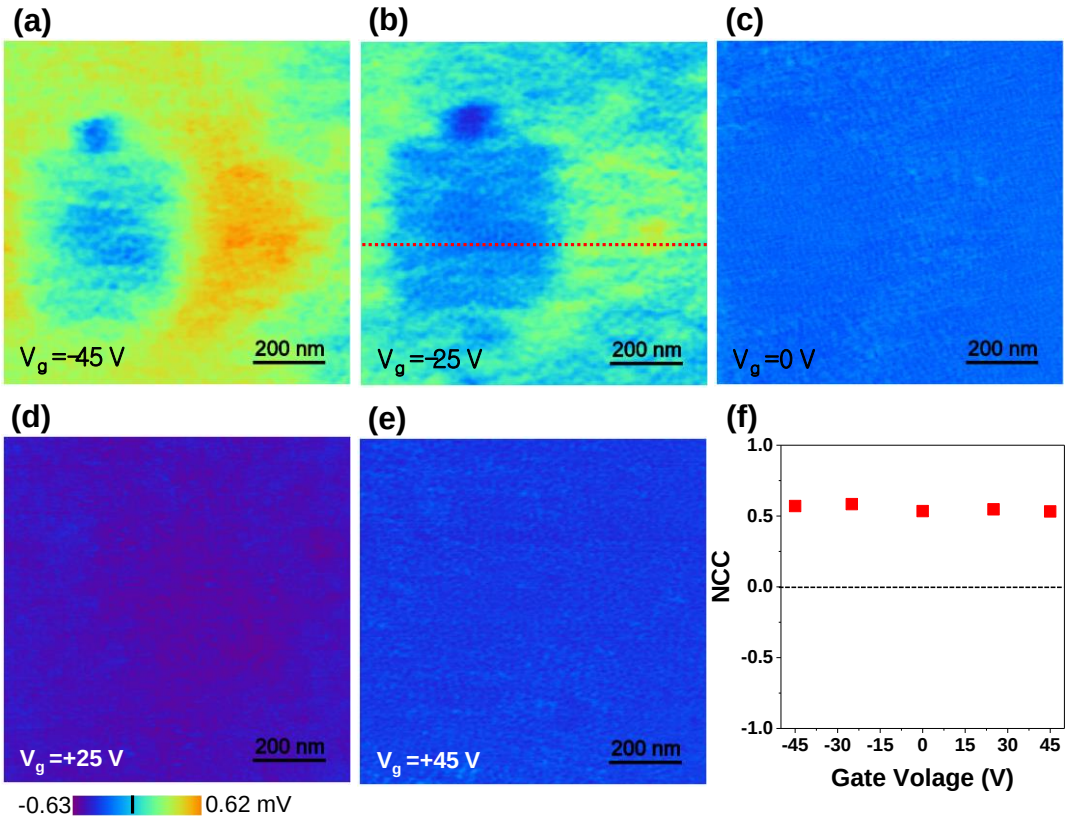

Figure S5. Strain-induced thermoelectric puddles in SLG (1.0 μm× 1.0 μm) at different back-gate voltages. From panel **(a)** to **(e)**, the back-gate voltages are -45 V, -25 V, 0 V, +25 V, and +45 V, respectively (ΔT=60 K). The corresponding topography image is shown in **Figure 3**a in the main text. **(f)** Normalized cross-correlation (NCC) between the topography and thermoelectric voltage mapping as a function of the gate voltage. The calculated NCC between the topography and thermoelectric voltage mapping is about 0.55 and varies little with the gate voltage, suggesting that the thermoelectric fluctuation is dominated by surface corrugation (strain).

6. Thermoelectric puddles in the ABA-stacked TLG at different back-gate voltages

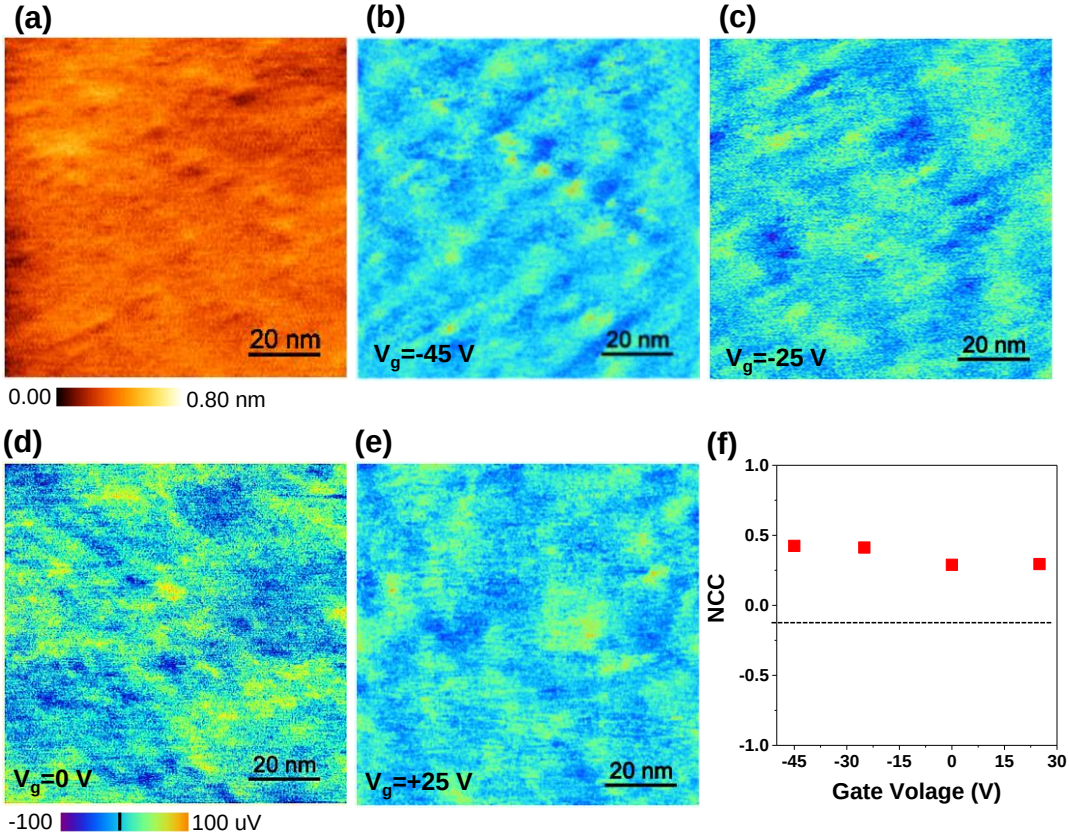

Figure S6. Thermoelectric puddles in the ABA-stacked TLG at different back-gate voltages. (a) Topography image of ABA-stacked TLG (100 nm×100 nm). **(b)-(e)** Thermopower mappings at the back-gate voltages of -45 V, -25 V, 0 V, and +25 V, respectively (ΔT=60 K). The scale bar represents the thermoelectric voltage deviation from the mean value in the scanned region. **(f)** NCC between topography and thermoelectric puddles with respect to the gate voltage. The calculated NCC is smaller than 0.5, and varies slightly with gate voltage, suggesting a certain correlation between topography and thermoelectric puddles in ABA-stacked TLG.

7. Thermoelectric puddles in the ABC-stacked TLG at different back-gate voltages

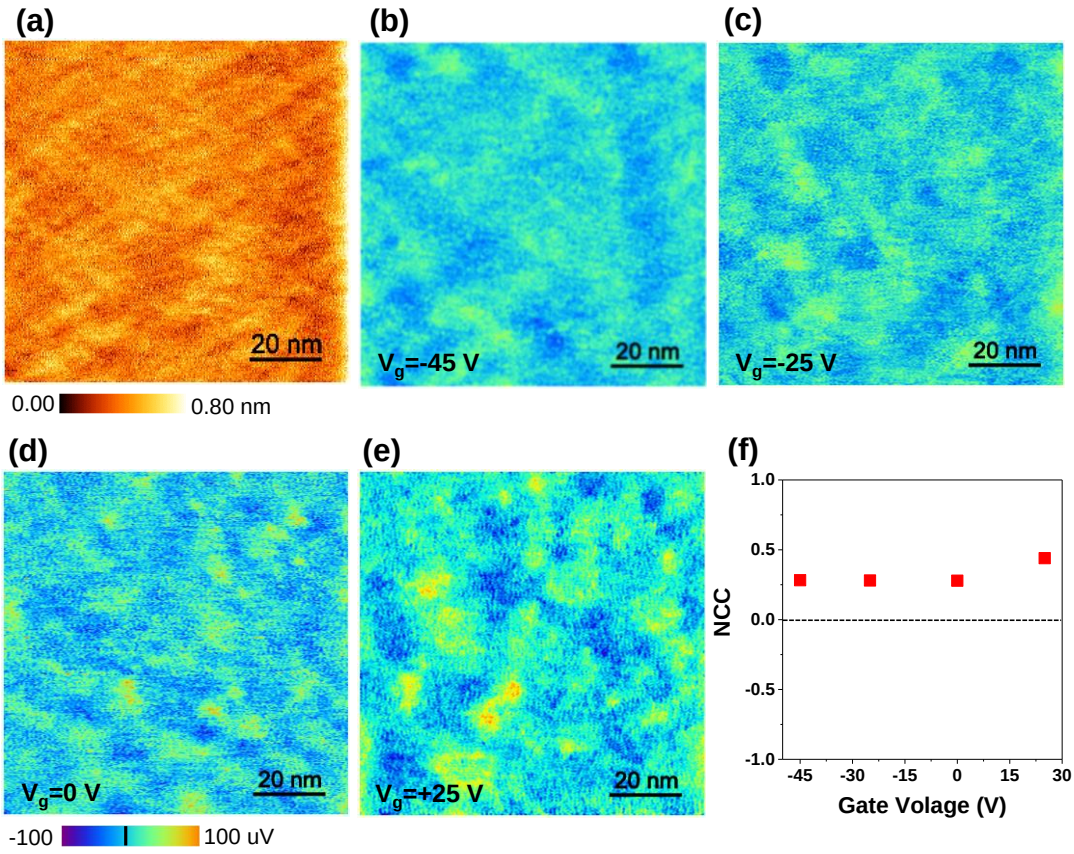

Figure S7. Thermoelectric puddles in the ABC-stacked TLG at different back-gate voltages. (a) Topography image of ABC-stacked TLG (100 nm×100 nm). **(b)-(e)** Thermopower mappings at the back-gate voltages of -45 V, -25 V, 0 V, and +25 V, respectively (ΔT=60 K). The scale bar represents the thermoelectric voltage deviation from the mean value in the scanned region. **(f)** NCC between topography and thermoelectric puddles as a function of the gate voltage.

8. Temperature dependent thermoelectric voltage mapping

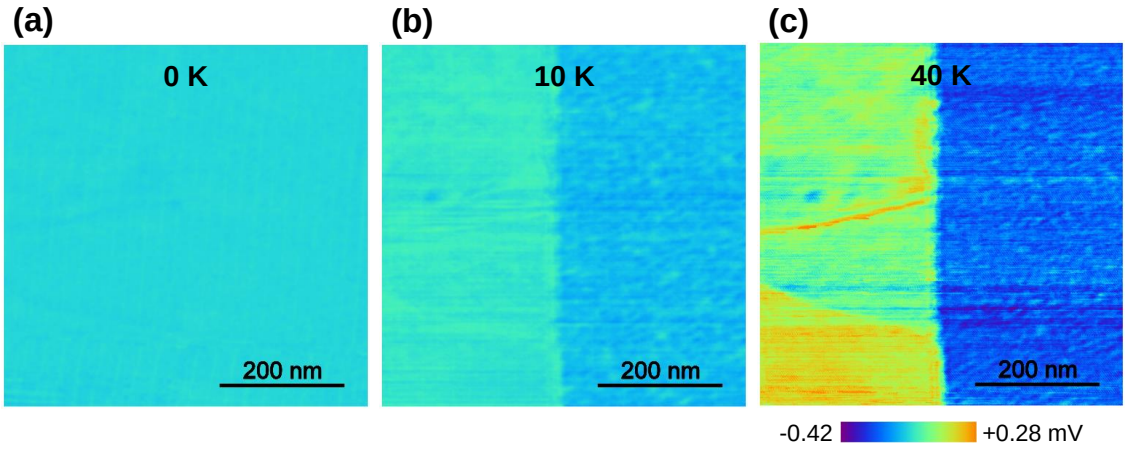

Figure S8. Temperature-dependent thermoelectric voltage mapping at a same region. From **(a)** to **(c)**, the temperature differences between the tip and sample are 0 K, 10 K, and 40 K, respectively. The contrast becomes weak as the temperature difference decreases.

REFERENCES

(1) Wang, H.; Wu, Y.; Cong, C.; Shang, J.; Yu, T. Hysteresis of Electronic Transport in Graphene Transistors. *ACS Nano.* **2010**, *4* (12), 7221-7228.

(2) Frank, O.; Tsoukleri, G.; Parthenios, J.; Papagelis, K.; Riaz, I.; Jalil, R.; Novoselov, K. S.; Galiotis, C. Compression Behavior of Single-Layer Graphenes. *ACS Nano.* **2010**, *4* (6), 3031-3138.

(3) Ni, Z. H.; Yu, T.; Lu, Y. H.; Wang, Y. Y.; Feng, Y. P.; Shen, Z. X. Uniaxial Strain on Graphene: Raman Spectroscopy Study and Band-Gap Opening. *ACS Nano.* **2008**, *2* (11), 2301-2305.

(4) Lee, J. E.; Ahn, G.; Shim, J.; Lee, Y. S.; Ryu, S. Optical Separation of Mechanical Strain from Charge Doping in Graphene. *Nat. Commun.* **2012**, *3* (1024), 1-8.

(5) Mueller, N. S.; Heeg, S.; Alvarez, M. P.; Kusch, P.; Wasserroth, S.; Clark, N.; Schedin, F.; Parthenios, J.; Papagelis, K.; Galiotis, C. Evaluating Arbitrary Strain Configurations and Doping in Graphene with Raman Spectroscopy. *2D Mater.* **2017**, *5* (1), 015016.

(6) Jung, S.; Rutter, G. M.; Klimov, N. N.; Newell, D. B.; Calizo, I.; Hight-Walker, A. R.; Zhitenev, N. B.; Stroscio, J. A. Evolution of Microscopic Localization in Graphene in a Magnetic Field from Scattering Resonances to Quantum Dots. *Nat. Phys.* **2011**, *7*, 245-251.

(7) Samaddar, S.; Yudhistira, I.; Adam, S.; Courtois, H.; Winkelmann, C. B. Charge Puddles in Graphene near the Dirac Point. *Phys. Rev. Lett.* **2016**, *116*, 126804.

(8) Choudhary, S. K.; Gupta, A. K. Effects of Tip Induced Carrier Density in Local Tunnel Spectra of Graphene. *Appl. Phys. Lett.* **2011**, *98*, 102109.

(9) Xu, R.; Yin, L.-J.; Qiao, J.-B.; Bai, K.-K.; Nie, J.-C.; He, L. Direct Probing Stacking Order and Electronic Spectrum of Rhombohedral Trilayer Graphene with Scanning Tunneling Microscopy. *Phys. Rev. B.* **2014**, *91*, 035410.

(10) Lui, C. H.; Li, Z.; Mak, K. F.; Cappelluti, E.; Heinz, T. F. Observation of an Electrically Tunable Band Gap in Trilayer Graphene. *Nat Phys.* **2011**, *7*, 944-947.

(11) Que, Y.; Xiao, W.; Chen, H.; Wang, D.; Du, S.; Gao, H.-J. Stacking-Dependent Electronic Property of Trilayer Graphene Epitaxially Grown on Ru(0001). *Appl. Phys. Lett.* **2016**, *107*, 263101.

(12) McElroy, K.; Lee, J.; Slezak, J. A.; Lee, D.-H.; Eisaki, H.; Uchida, S.; Davis, J. C. Atomic-Scale Sources and Mechanism of Nanoscale Electronic Disorder in $Bi_2Sr_2CaCu_2O_8$+delta. *Science.* **2005**,

309 (5737), 1048-1052.